

## Resonant seismic emission of subsurface objects

Valeri Korneev<sup>1</sup>

### ABSTRACT

Numerical modeling results and field data indicate that some contrasting subsurface objects (such as tunnels, caves, pipes, filled pits, and fluid-filled fractures) are capable of generating durable resonant oscillations after trapping seismic energy. These oscillations consist of surface types of circumferential waves that repeatedly propagate around the object. The resonant emission of such trapped energy occurs primarily in the form of shear body waves that can be detected by remotely placed receivers. Resonant emission reveals itself in the form of sharp resonant peaks for the late parts of the records, when all strong direct and primary reflected waves are gone. These peaks were observed in field data for a buried barrel filled with water, in 2D finite-difference modeling results, and in the exact canonical solution for a fluid-filled sphere. A computed animation for the diffraction of a plane wave upon a low-velocity elastic sphere confirms the generation of resonances by durable surface waves. Resonant emission has characteristic quasi-hyperbolic traveltimes patterns on shot gathers. The inversion of these patterns can be performed in the frequency domain after muting the strong direct and primary scattered waves. Subsurface objects can be detected and imaged at a single resonance frequency without an accurate knowledge of source trigger time. The imaging of subsurface objects requires information about the shear velocity distribution in an embedding medium, which can be done interactively during inversion.

### INTRODUCTION

Some contrasting acoustic and elastic objects, such as tunnels (of different kinds), pipes, buried containers, unexploded ordnances (UXO), mine shafts, and fluid-filled fractures, are capable of resonating at certain frequencies as a result of trapping energy from passing waves and slowly releasing that energy back into an outer medium. As high-contrast scatterers, these objects are capable of generat-

ing strong scattered waves in which primary (ballistic) PP, PS, and SS reflected and converted waves carry away most of the energy brought in by the incident waves. This conclusion follows from numerical and analytic results obtained from the canonical solutions for spheres and cylinders (Uberall, 1973; Frisk et al., 1975; Met-saveer et al., 1979; Veksler, 1980, 1984; Korneev and Johnson, 1996), and practically all scientific work done in determining underground scatterers relies on the use of these waves (e.g., Landa and Keydar, 1998; Groenenboom and Falk, 2000). Apart from the primary scattered waves, canonical solutions also predict the existence of other waves, which creep along the walls of an object while emitting secondary scattered energy into an embedding medium.

Waves that propagate around an object along its outer interface are called circumferential waves. Emissions coming from propagating circumferential waves have been studied intensively in hydroacoustic problems (Uberall, 1973; Frisk et al., 1975; Veksler, 1980, 1984) and found to have two distinct features compared with a typical seismological application. First, the embedding medium in hydroacoustics is water, which is relatively homogeneous and conducts no shear waves. Second, in hydroacoustic applications, the source and receiver are located at the same point, and therefore the recorded signals represent a backscatter energy called echo signals. These simplifying features, as well as the high practical importance of echolocating problems, have resulted in thorough analytic and numerical studies of echo-signal compositions.

Four types of circumferential waves are known. The first type is the Frantz wave (Frantz, 1954), which propagates around the object with velocity approximately equal to that of the embedding medium. These waves merge with direct waves in the edges of shadow zones and form most of the wavefield in these zones (Groenenboom and van Dam, 2000). Frantz waves intensively radiate energy into the outer medium and rapidly decay in amplitude over time. The second type consists of “whispering gallery” waves (Rayleigh, 1924), which primarily propagate inside an object being multiply reflected from a curved object’s interface. Whispering gallery waves also decay rapidly because they lose energy during reflections at interfaces.

Manuscript received by the Editor 24 March 2008; revised manuscript received 2 September 2008; published online 10 March 2009; corrected version published online 23 March 2009.

<sup>1</sup>Lawrence Berkeley National Laboratory, Earth Sciences Division, Berkeley, California, U.S.A. E-mail: vakorneev@lbl.gov.  
© 2009 Society of Exploration Geophysicists. All rights reserved.

The third type of circumferential wave is the Rayleigh. Even if their initial amplitude is small compared with other waves, over a long observation time Rayleigh waves can dominate in records, as happens with teleseismic events. Finally, the fourth type, Stoneley waves, can be excited when either the object or medium is a fluid (Uberall, 1973). Stoneley waves also are slowly decaying waves, and they can make many propagation cycles around an object without significant attenuation.

For high- and low-velocity objects, the primary scattered waves have the same order of magnitude. The main difference between these objects is in the later arrivals, after all primary waves are gone. Whereas high-velocity objects effectively radiate most of their energy soon after an impact, low-velocity objects trap some fraction of the energy in the form of multiple reflections. High-contrast objects of both types also support circumferential waves that slowly release their energy by radiating common body waves. The resonant character of echo signals was observed both in data and numerically. Sharp spectral peaks of these signals appear because of the slow amplitude decay of circumferential waves, when an object's geometry allows a constant rotation time around it.

Circumferential waves have been studied in an elastic outer medium, primarily for objects with cylindrical symmetry (Plona, et al., 1992; Hassan and Nagy, 1997). Applications include pipe testing and borehole-condition analysis. In fluid-filled fractures with finite lengths, resonances can be supported by the slow Stoneley guided waves (Korneev, 2008). However, observations and numerical simulations of these resonances are yet to be developed. This study demonstrates that resonant emission can be detected in both real and synthetic data. After simple processing, seismic emission records can be

used effectively for seismic imaging and velocity estimations. The remarkable feature of resonant seismic emission is that it consists predominantly of shear body waves.

## FIELD EXPERIMENT

### Experimental setup and data acquisition

The field experiment (described in this paper), conducted in 1999, was intended to generate the test data set for subsurface object-detection and imaging methods. Soil for the experiment consisted of compacted, consolidated sand with a P-velocity of 500 m/s and an S-velocity of 240 m/s. The object was a water-filled barrel 60 cm in diameter and 120 cm in height. Some air bubbles were left inside the barrel before it was sealed. The barrel was placed at a depth of 5–6 m in a specially excavated pit, which then was backfilled with soil. A 24-channel 0.5-m spaced line of vertical geophones was used for every ground shot made by a sledgehammer, with a shotpoint positioned at the first receiver of each line (Figure 1). There were 87 shots in total at a 1-m spacing interval. The middle receiver of line 51 was directly above the barrel. The records were 0.5 seconds in length with a 0.5-ms data sampling rate.

Figure 2 shows raw shot gathers 45–57. Direct P- and S-waves have dominating amplitudes on each trace, and from 0.1 seconds after first arrivals, no coherent waves were visible in the data (Korneev and Landa, 2007). No primary scattered waves are visible in the background of the direct waves. (Some waves can be interpreted as reflections from the pit.) We are unaware of any successful attempts to detect and image the barrel using these data.

### Imaging

After applying automatic gain control (AGC) with a 25-ms window, the late (0.25–0.5-s) interval revealed sharp resonant peaks in amplitude spectra at frequency  $f_{\text{res}} = 78$  Hz (Figure 3). Band-pass filtering of traces in the 75–83-Hz interval yielded the clear hyperbolic signature of a secondary seismic source with the apex in the middle of line 51 (Figure 4). The phase slopes (240 m/s) of the secondary source correspond to the velocity  $V_s$  of shear waves in an embedding medium.

If a velocity is known, single-shot information is enough to locate the barrel. The apex location points at the horizontal coordinate. Fitting the hyperbolic curvature allows us to determine the barrel's depth. Using information from all available data, we consider modeling the Green's function  $W_{nk}(f)$  in the form

$$W_{nk}(f_{\text{res}}) = \exp(i2\pi f_{\text{res}}\tau_{nk})/r_{nk}, \quad (1)$$

which describes the monochromatic wavefield excited by an underground secondary source at the point  $M_k \equiv M_k(x_k, z_k)$  with spatial coordinates  $x_k, z_k$ , and record at the sensor location  $S_n \equiv S_n(x_n, z_n)$ , where  $r_{nk}$  is the wave travel distance between points  $M_k$  and  $S_n$ , and  $i = \sqrt{-1}$ . Travel-times  $\tau_{nk}$  were computed assuming a homogeneous velocity

$$\tau_{nk} = \frac{r_{nk}}{V_s}. \quad (2)$$

The imaging function was taken to be of the form

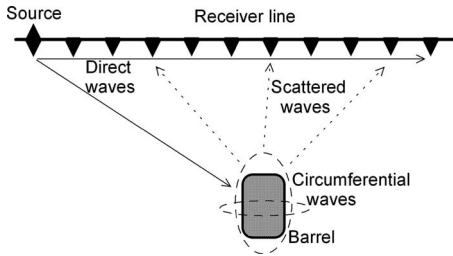


Figure 1. Geometry of the seismic experiment to locate a buried water-filled barrel. Solid lines, dashed lines, and dotted-line arrows indicate direct, circumferential, and scattered waves, respectively.

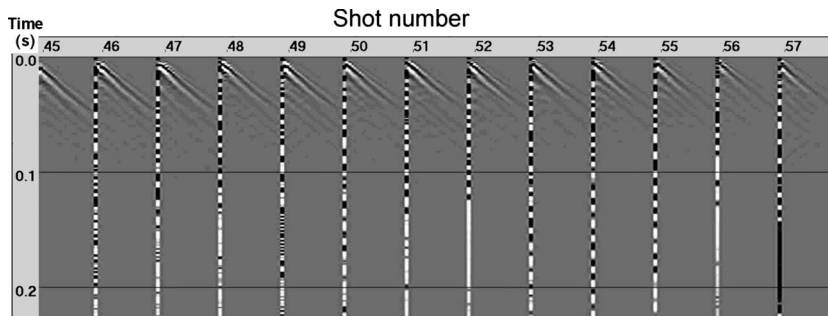


Figure 2. Shot gathers 45–57 for field data recorded above the buried barrel. The direct S-wave is visible. Barrel is located in the middle of gather 51. Contrasting black-and-white striped lines correspond to the first receivers for each shot that are coincident with source positions.

$$F(M_k) = \sum_j \left| \sum_{n=1}^N s_{nj}^*(f_{\text{res}}) W_{nk}(f_{\text{res}}) \right|, \quad (3)$$

where  $s_{nj}(f_{\text{res}})$  is the spectral component of data from shot  $j$  recorded in receiver  $n$  ( $1 \leq n \leq N$ ) and contained in the 0.3–0.4-s-time interval from Figure 4. The star (\*) denotes complex conjugation. The summation in equation 3 covers all shots in the vicinity of the imaging area (shots 45–57).

The use of absolute values in equation 3 makes the inversion independent of shot-origin times and stabilizes the inversion result, which is shown in Figure 5. A similar inversion was performed in the time domain, but it required phase picking, which generally is an unstable and nonunique procedure. The implementation of equation 3 is simple, straightforward, and quick. The maximum value zone in Figure 5 indicates the barrel's correct location and contains contributions from all shots used. To ensure the best image quality, the inversion was performed for different velocities  $V_s$  in the 200–300-m/s range. At incorrect velocities, the inversion image smears and splits in several anomalies. The best focusing was obtained for  $V_s = 235$  m/s. Thus, the described imaging approach enables the evaluation of imaging velocities.

## Modeling

We modeled the field data with a 2D elastic finite-difference code, using a  $40 \times 12.5$  m model with 0.05-m grid spacing. The background  $V_p$  and  $V_s$  velocities had the same values as in the field experiment. The local object was modeled as a  $1 \times 0.7$  m rectangular inhomogeneity containing fluid with 70 m/s velocity and  $1 \text{ g/cm}^3$  density. Ten shot gathers were computed using 3-m spacing for sources. The surface receiver line was the same for all shots and had 61 sensors separated by 0.5 m. A single shot gather for shot 3 is shown in Figure 6, in which (similarly to the field case) the primary scattered waves rapidly decay after 0.2 s. The recording length was 1 s. A snapshot image at 0.3 s (Figure 7) shows that at a late propagating time, the field predominantly consists of shear waves created by circumferential waves in the object. The spectral content of later parts of the records (after 0.5 s) shows a sharp peak at 53 Hz in all traces (Figure 8).

All data were subjected to AGC and were band-pass filtered around the peak frequency, leading to the images shown in Figure 9 and revealing quasi-hyperbolic phases similar to those observed in the real data (Figure 4). Application of the inversion procedure described in the previous section revealed a clear image of the heterogeneity (Figure 10).

## NUMERICAL EXPERIMENT: RESONANT SPHERE

### General considerations

Spherical models allow for analytic scattering solutions and therefore can be helpful in understanding the basic properties of scattered fields formed on less treatable objects. Following the general formulation for diffraction upon a sphere (Korneev and Johnson, 1996), we present here some numerical results that illustrate the resonant scattering mechanism. An integral scattering

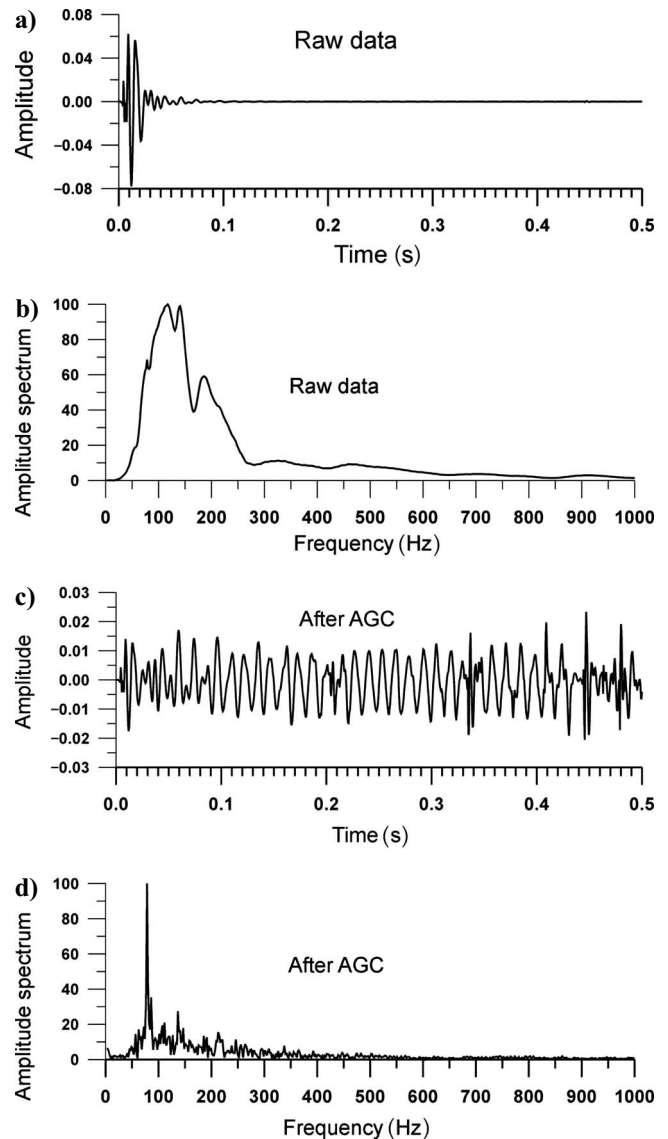


Figure 3. (a) Single seismic trace recorded at surface over a buried water-filled barrel. (b) Amplitude spectrum of trace in (a). (c) Result of applying AGC to trace in (a). (d) Amplitude spectrum of trace in (c). Durable oscillation in late arrivals primarily consists of single harmonic at 78 Hz.

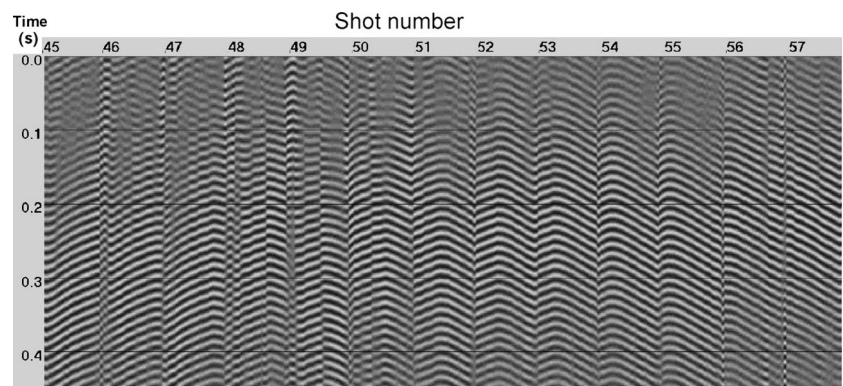


Figure 4. Shot gathers 45–57 after AGC and band-pass filtering around 78 Hz show hyperbolic monochromatic signatures of a secondary source. Hyperbola's apex indicates lateral position of the object. Its curvature has direct relationship with object's depth.



characteristic called the “normalized scattering cross section,”  $\sigma_w$ , ( $W = P, S$ ), relates the total energy of the scattered field to the energy of a P- or S-wave incident upon the object. For an elastic embedding medium, partial P- and S-scattering cross sections  $\sigma_{PW}$  and  $\sigma_{SW}$ , ( $W = P, S$ ) can be considered, which correspond to separate

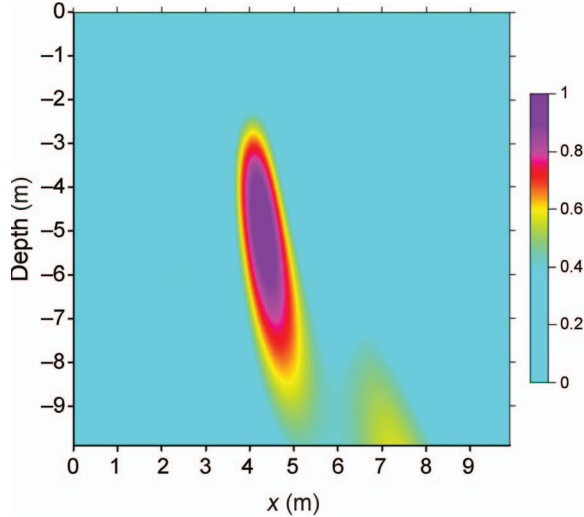


Figure 5. Migrated image of the buried barrel. Displayed is the function  $F$  from equation 3.

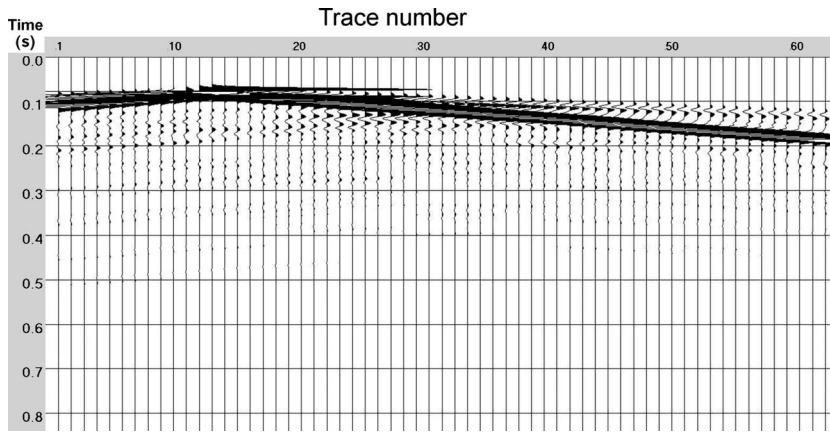


Figure 6. Single shot gather 3 for vertical component of the modeled traces. Amplitudes rapidly decay after first arriving phases.

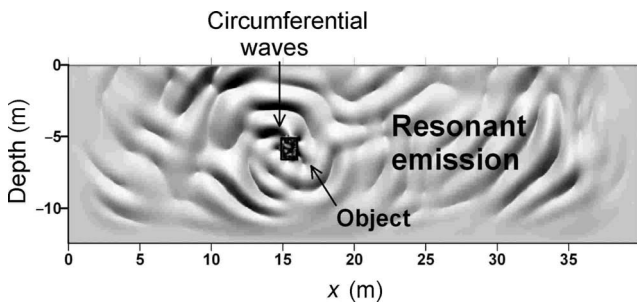


Figure 7. Shaded relief snapshot at 0.8 s shows circumferential waves rotating around the object. These waves cause resonant emission (waves) propagating in embedding medium.

contributions of compressional and shear scattered waves. It has been shown (Korneev and Johnson, 1996) that for any spherical object,

$$\frac{\sigma_{PS}}{\sigma_{SP}} = 2 \frac{V_P^4}{V_S^4}, \quad (4)$$

and the seismic energy primarily converts into shear waves. In equation 4, the velocities on the right-hand side correspond to the embedding medium.

## Results

Figure 11 shows  $\sigma_{PP}$  and  $\sigma_{PS}$  partial scattering cross sections for a fluid-filled sphere. The sphere has a radius of  $R = 0.5$  m, and the fluid is characterized by  $V_f = 110$  m/s and a density of  $1$  g/cm<sup>3</sup>. This model reflects the case in which the liquid contains some gas bubbles; such a mixture has the compressibility of gas and density of liquid. Such a parameter combination leads to very low propagation velocities (Kaelin, 1998), which are lower than those in the embedding shallow subsurface. The chosen parameter set shows a sharp resonant peak at 78 Hz, which coincides with the peak in real data (Figure 3). For P and S types of incident waves, the scattering energy of S-waves overwhelms the energy of P-waves, which apparently can be neglected in real applications. The first resonant peaks for a fluid-filled sphere follow the equation (Korneev and Johnson, 1996)

$$j_2(\xi) - \frac{j_1(\xi)}{\xi} = 0, \quad \xi = \frac{\omega R}{V_f}, \quad (5)$$

containing the spherical Bessel functions  $j_k(\xi)$  and frequency  $\omega$ . The first three roots of this equation are  $\xi = 2.1, 5.9$ , and  $9.2$ . Thus, if resonance frequency is measured and velocity  $V_f$  is known, the radius of the sphere  $R$  can be determined using equation 5.

## Animation

A solution for the sphere also was used to compute an animation of plane P-wave diffraction upon an elastic low-velocity sphere. This sphere has a 1-m radius, a material with  $V_P = 4500$  m/s,  $V_S$  of 2600 m/s, and a density of  $2.3$  g/cm<sup>3</sup>. The embedding medium has corresponding parameters  $V_P = 6000$  m/s,  $V_S = 3500$  m/s, and density =  $2.7$  g/cm<sup>3</sup>. The  $6 \times 6$  m frame was filled with a grid of pixels with 2-cm spacing. For each pixel, a 0.256-s-long trace was computed by Fourier transforming an analytic solution formulated in a frequency domain. Two time slices of the  $z$ -component are shown in Figure 12 for (a)  $t_1 = 0.001$  s and (b)  $t_2 = 0.002$  s. The animation is computed for a P-plane incident wave. No assumptions about the boundaries other than sphericity are used. At the early time (a), the wavefield consists of geometrically interpretable reflected and refracted waves; at the late time (b), the dominant feature represents Rayleigh circumferential waves. Shorter S-waves penetrate deeper into the sphere, whereas P-waves propagate close to the sphere interface.

Figure 13 shows  $x$ - and  $z$ -components of a diffracted field caused by a plane P-wave incident upon a low-velocity elastic sphere. To

maintain a dynamic resolution of the frames, a variable color scale was applied. The sphere has a regular “heartbeat” at late times. These oscillations correspond to resonances caused by circumferential waves.

## DISCUSSION

The imaging of shallow subsurface heterogeneities has a variety of important applications, including the detection and location of seismically contrasting objects. The primary scattered waves from such target objects could be used for object imaging; however, these waves closely interfere with other strong waves, making such imaging difficult. Resonant emission waves have relatively small amplitudes, but they are much more durable than primary scattered waves. Extraction of the resonant emission waves from late arrivals makes it possible to detect and image subsurface objects, using data at resonance frequencies. Resonant emission propagates in the embedding media primarily in the form of shear body waves, which is distinct from the hydroacoustic case. This follows from the canonical solutions, reflecting the fact that S-waves are slower than P-waves and that wave energy preferably converts into slow-velocity waves.

The imaging of resonating objects implements wave-migration ideas in a frequency domain. It uses the assumption that every underground location potentially contains a monochromatic source radiating seismic waves. In elastic media, these radiated waves mostly consist of shear waves. The possibility of neglecting P-waves for inversion purposes makes imaging simple, robust, and practically insensitive to the size and extent of the data-selection window. No data picking is necessary for inversion. In the case of several objects with different resonating frequencies, the objects can be imaged consecutively at each frequency. Knowledge about shear-wave velocity in the embedding medium seems essential for a successful inversion. However, the relatively fast (seconds) inversion computation makes it possible to perform this inversion for a range of reasonable velocity distributions. A correct velocity distribution provides the sharpest localized image.

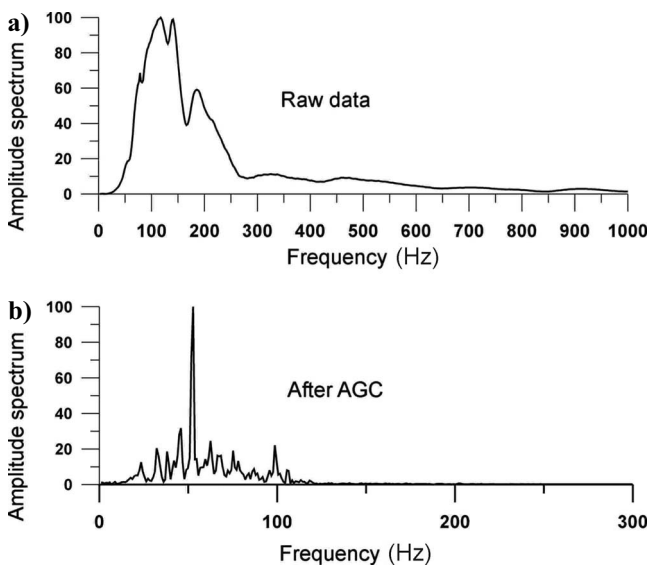


Figure 8. (a) Amplitude spectrum of trace 30 from the shot gather shown in Figure 6. (b) Amplitude spectrum of the same trace as on (a) but after applying AGC reveals sharp peak at 53 Hz, similar to results for filed data from Figure 3.

In practice, several classes of objects contain elements with contrasting velocities that differ significantly from those in the embedding media (tunnels, pipes, mine shafts, and cavities filled with gas, ice lenses, metallic objects, UXO, and so forth). The high contrasts of such structures result in durable circumferential waves (primarily of the Stoneley type in fluid-filled structures, and of the Rayleigh type in elastic structures). Another class of wave-trapping objects consists of localized low-velocity zones that have naturally low velocity (as part of a coal seam) or that result from some impact, such as filled excavation pits, where loosened rock/soil has smaller elastic moduli compared with the embedding medium. The intrinsic attenuation inside an object is a likely contributor to the decrease rate of wave amplitude.

A single object can have a set of resonant frequencies. The values of resonant frequencies depend on the object's size and material properties. When constraints are imposed on some of the object parameters, the resonant frequencies can be inverted for the remaining parameters, using analytic solutions, numerical modeling, or calibration measurements. Indeed, if the object has a closed geometry enabling the surface wave to return to its original position after full rotation around the object, then the resonant period is simply the time difference between two consecutive rotations, and it stays constant during the whole process. This period is defined by the length of the object's perimeter and the propagation velocity, and it can be evaluated using the canonical wave-propagation solutions for an appropriate geometry. Knowledge about the resonance frequency and circumferential-wave velocity enables the estimation of perimeter length, giving the object's size for known shapes in a similar manner to the spherical example.

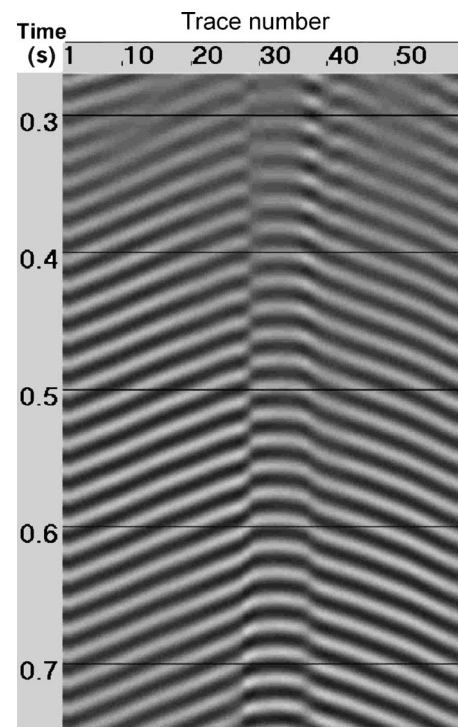


Figure 9. Late arrivals of modeled data after applying AGC and band-pass filtering around the resonance frequency have a repeating quasi-hyperbolic pattern similar to one observed for field data (Figure 4).

Figure 10. Migrated image of the modeled data locates the object and is similar to one obtained from field data (Figure 5).

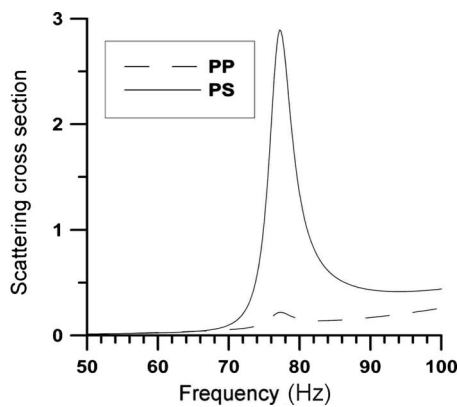
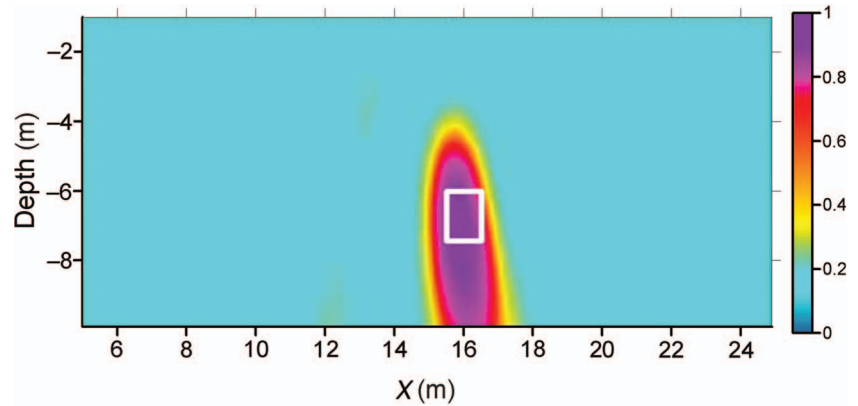


Figure 11. Scattering cross section for a fluid-filled sphere with a resonant peak at 78 Hz.

Another important characteristic of resonant emission is the width of the resonant peak and the decay rate in the time domain. Both phenomena describe resonant-emission attenuation that likely depends on the material parameters of an object and an embedding medium, as well as on the shape of the object's interface. The detailed study of such dependences is beyond the scope of this paper.

As for any new imaging approach, it should be considered for reservoir-imaging applications. If the reservoir consists of flat sedimentary layers, then only reflected waves can be recorded from them. Multiple reflections from such structures (although very periodic in time) rapidly decay in amplitude, making their detection at late times nearly impossible. However, some structural hydrocarbon traps with local heterogeneities possibly could develop resonances and be imaged by using the method described in this paper.

Fluid-filled fractures also can resonate and therefore be imaged using resonant emission. As recently shown in Korneev (2008), Stoneley guided waves for realistic fracture and fluid parameters have very low velocities and a large enough attenuation factor  $Q$  to propagate many wavelengths without significant attenuation. In particular, a 1-mm-thick water/oil-filled fracture resonates at frequency as low as 10 Hz when the fracture is just 4 m long. Stoneley guided waves do not radiate body waves during propagation until they scatter on fracture tips, which become the origins of secondary sources and generate body waves, which potentially could be used for fracture imaging. Such radiation was detected and explained (Chouet, 1986; Ferrazzini and Aki, 1987) as being caused by the oscillation of

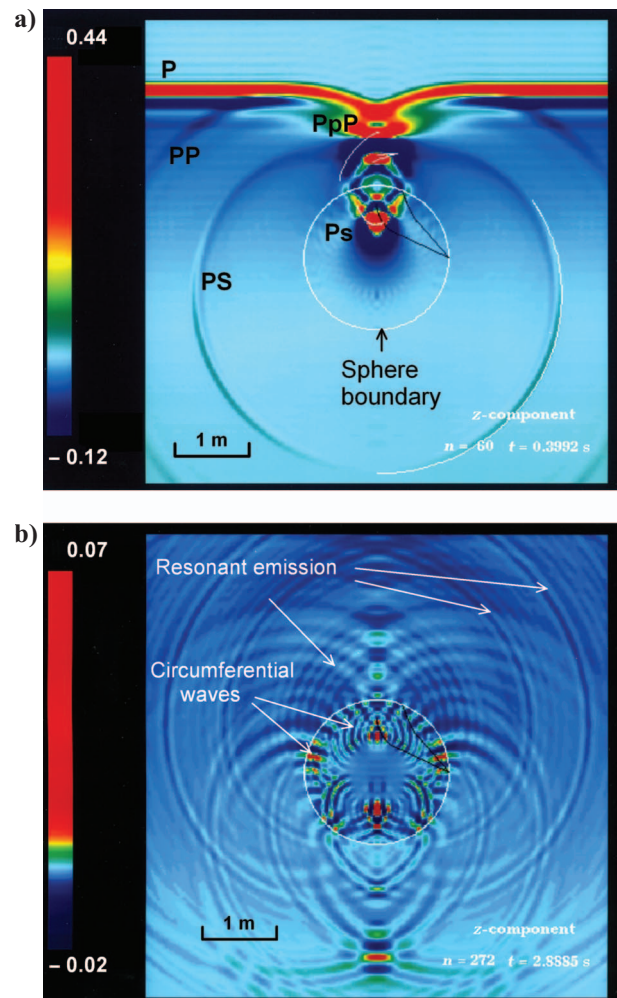


Figure 12. Snapshots of field  $z$ -component for the low-velocity elastic sphere at 0.001 ms (a) when just primary scattered waves are formed, and at 0.02 ms (b) when just circumferential (Rayleigh) waves dominate the wavefield.

volcanic molten lava. This oscillation can be excited by fracture propagation or by microseismic or teleseismic events. The monitoring of these oscillations should reveal information about the fracture dynamic and growth because the resonance frequencies and location of radiation points change along with fracture geometry changes.



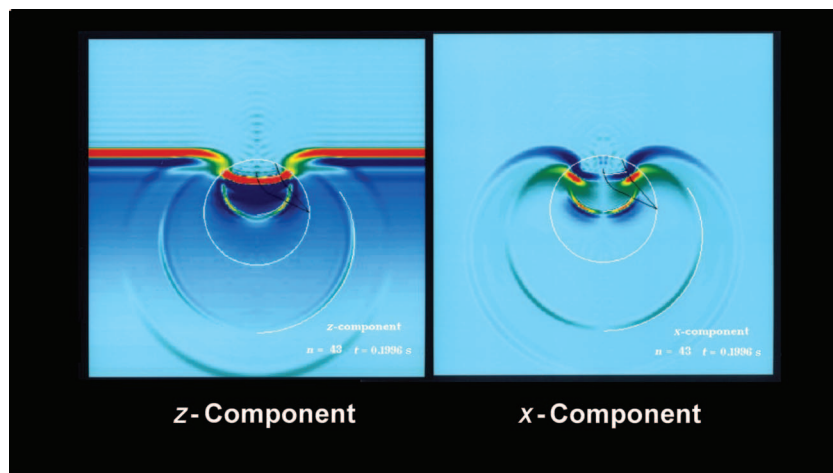


Figure 13. Snapshot of animation showing  $x$ - and  $z$ -components of a diffracted field caused by a plane  $P$ -wave incident upon low-velocity elastic sphere. A periodic pulsation of the field occurs at late times. Figure is enhanced online. [DOI: <http://dx.doi.org/10.1190/1.3068448.1>]

## CONCLUSIONS

Low-velocity subsurface heterogeneities trap seismic energy and can release it long after the recordings of primary scattered waves. Trapped energy primarily consists of circumferential waves propagating along the perimeter of an object, and this energy radiates in the surrounding medium as body waves. Circumferential waves propagate in both directions around an object, which potentially could create discontinuous traveltimes. Most of the energy radiated back to the embedding medium is carried by shear waves. This simple data pattern makes it an attractive candidate for inversion techniques based on migration (back-propagation) principles. Unlike conventional diffraction-imaging techniques, resonant-emission imaging can be performed at a single frequency and does not require accurate information about source position. There also is no need to engage in laborious wave-separation preprocessing, because all primary waves can simply be muted.

We expect that multiple objects could be detected and imaged using separation in the frequency domain. Moreover, objects with the same resonant frequencies should be possible to resolve spatially if they have distinctly different phase functions in receiver locations. Limits of the spatial resolution are defined by imaging wavelength similarly to common optical images. Clearly, the exact timing of a source excitation is not important: trapped energy radiation possibly could be observed in the presence of background noise, leading to cost-effective object-detection techniques. Requirements on the sensor coverage are yet to be estimated. Overall, the new object-detection method shows a good correspondence between field and

modeled data. In its current formulation, the method is ready for extensive testing and tuning.

## ACKNOWLEDGMENTS

This work was supported by the National Energy Technology Laboratory, Office of Fossil Energy Sciences of the U. S. Department of Energy under Contract No. DE-AC02-05CH11231. Field data were provided by Eugeny Landa (OP-ERA); GeoKinetik, LLC, provided Kinetik Professional processing software.

## REFERENCES

- Chouet, B., 1986, Dynamics of a fluid-driven crack in three dimensions by the finite-difference method: *Journal of Geophysical Research*, **91**, 13967–13992.
- Ferrazzini, V., and K. Aki, 1987, Slow waves trapped in a fluid-filled infinite crack: Implications for volcanic tremor: *Journal of Geophysical Research*, **92**, 9215–9223.
- Frantz, W., 1954, Über die Greenschen Funktionen des Zylinders und der Kugel: *Z. Naturforschung*, **9a**, 705–716.
- Frisk, G. V., J. W. Dickey, and H. Uberall, 1975, Surface wave modes on elastic cylinders: *Journal of Acoustical Society of America*, **58**, no. 5, 996–1008.
- Groenenboom, J., and J. Falk, 2000, Scattering by hydraulic fractures: Finite-difference modeling and laboratory data: *Geophysics*, **65**, 612–622.
- Groenenboom, J., and D. B. van Dam, 2000, Monitoring hydraulic fracture growth: Laboratory experiments: *Geophysics*, **65**, no. 2, 603–611.
- Hassan, W., and P. B. Nagy, 1997, Circumferential creeping waves around a fluid-filled cylindrical cavity in an elastic medium: *Journal of Acoustical Society of America*, **101**, 2496–2503.
- Kaelin, B., 1998, Seismic imaging of the shallow subsurface with high-frequency seismic measurements: Ph.D. thesis, University of California, Berkeley.
- Korneev, V. A., 2008, Slow waves in fractures filled with viscous fluid: *Geophysics*, **73**, no. 1, N1–N7.
- Korneev, V. A., and L. R. Johnson, 1996, Scattering of  $P$  and  $S$  waves by spherically symmetric inclusion: *Pure and Applied Geophysics*, **147**, 675–718.
- Korneev, V. A., and E. Landa, 2007, Imaging of subsurface objects using resonant seismic scattering, 77th Annual International Meeting, SEG, 1113–1117.
- Landa, E., and S. Keydar, 1998, Seismic monitoring of diffraction images for detection of local heterogeneities: *Geophysics*, **63**, 1093–1100.
- Metsaveer, Y. A., N. D. Veksler, and A. S. Stulov, 1979, Diffraction of acoustic pulses on elastic bodies (in Russian): Nauka.
- Plona, T. J., B. K. Sinha, S. Kostek, and S. K. Chang, 1992, Axisymmetrical wave propagation in fluid-loaded cylindrical shells: 2 — Theory versus experiment: *Journal of the Acoustical Society of America*, **92**, 1144–1155.
- Rayleigh, L., 1924, The problem of whispering gallery: *Philosophical Magazine*, **27**, 100–115.
- Uberall, N., 1973, Surface waves in acoustics, in M. P. Mason, and P. N. Thornston, eds., *Physical acoustics*: Academic Press 10, 1–60.
- Veksler, N. D., 1980, Scattering of pulses on elastic cylinders (in Russian): Tallinn, Valgus.
- , 1984, Resonant scattering in hydroacoustics (in Russian): Tallinn, Valgus.